QCD analysis of CMS W + charm measurements at LHC with $\sqrt{s}$ = 7 TeV and implications for strange PDF*

Nijat Yalkun[1,2]   Sayipjamal Dulat[1;1)]

[1]School of Physics Science and Technology, Xinjiang University, Urumqi, Xinjiang 830046 China
[2]Institute of Theoretical Physics, Chinese Academy of Sciences, Beijing 100190, China

Abstract: We calculate cross-sections and cross-section ratios of a charm quark production in association with a W gauge boson at next-to-leading order QCD using MadGraph and CT10NNLO, CT14NNLO, and MSTW2008NNLO PDFs. We compare the results with measurements from the CMS detector at the LHC at a center-of-mass energy of 7 TeV. Moreover, we calculate absolute and normalized differential cross-sections as well as differential cross-section ratios as a function of the lepton pseudorapidity from the W boson decay. The correlation between the CT14NNLO PDFs and predictions for W+ charm data are studied as well. Furthermore, by employing the error PDF updating method proposed by the CTEQ-TEA group, we update CT14NNLO PDFs, and analyze the impact of CMS 7 TeV W+ charm production data to the original CT14NNLO PDFs. By comparison of the $g(x,Q)$, $s(x,Q)$, $u(x,Q)$, $d(x,Q)$, $\bar{u}(x,Q)$, and $\bar{d}(x,Q)$ PDFs at Q = 1.3 GeV and Q = 100 GeV for the CT14NNLO and CT14NNLO+Wc, we see that the error band of the $s(x,Q)$ PDF is reduced in the region $x < 0.4$, and the error band of $g(x,Q)$ PDF is also slightly reduced at region $0.01 < x < 0.1$.

Keywords: parton distribution functions, W+ charm production

PACS: 12.15.Ji, 12.38.Cy, 13.85.Qk   **DOI:** 10.1088/1674-1137/43/12/123101

1 Introduction

In the standard model (SM), the associated W+ charm production in hadron collisions is described at leading order (LO) in perturbative quantum chromodynamics (QCD) by $g + q \rightarrow W^- + c$, $(q = d,s,b)$ and $g + \bar{q} \rightarrow W^+ + \bar{c}$, $(\bar{q} = \bar{d}, \bar{s}, \bar{b})$. Although the d-quark parton distribution function (PDF) is large in the proton, the processes $g + d \rightarrow W^- + c$ and $g + \bar{d} \rightarrow W^+ + \bar{c}$ contribute only about 10% [1] to the total W+ charm production rate, because it is suppressed by the small quark-mixing Cabibbo-Kobayashi-Maskawa (CKM) matrix element [2] $|V_{cd}|$ and $|V_{\bar{c}\bar{d}}|$. The major contribution to the total W+ charm production rate is due to strange quark-gluon fusion $g + s \rightarrow W^- + c$, and $g + \bar{s} \rightarrow W^+ + \bar{c}$. The contribution from $g + b \rightarrow W^- + c$ and $g + \bar{b} \rightarrow W^+ + \bar{c}$ is also heavily suppressed by the quark mixing matrix elements ($|V_{cb}|$, $|V_{\bar{c}\bar{b}}|$) and the b-quark PDF. The W+ charm production cross-section is therefore particularly sensitive to the proton $g(x,Q)$ and $s(x,Q)$

PDFs [3] and to the magnitude of the CKM matrix element V_{cs}, where x is the momentum fraction of the proton carried by the s-quark, and Q is the hard scale. The study cited in Ref. [4] calculated the W+ charm production at LO and next-to-leading order (NLO) in QCD, and found that the factorization and renormalization scale uncertainty in the NLO calculation is about 20%. Ref. [5] explored the strangeness degrees of freedom in the parton structure of the nucleon within the global analysis framework, and showed that the precise determination of the $s(x,Q)$ PDF affects the W+ charm cross-section. The $s(x,Q)$ PDF has been determined by neutrino-nucleon deep inelastic scattering experiments at momentum transfer squared $Q^2 = 10$ GeV, and momentum fraction $x \sim 0.1$ [6, 7]. The Tevatron CDF [8] and D0 [9] experiments have measured the cross-section for charm quark produced in association with W bosons, using muon tagging of the charm-quark jet. The ATLAS collaboration [10] measured the total cross-section, differential cross-section as a function of the pseudorapidity of the lepton from

the W boson decay, and the cross-section ratio of the production of a W boson in association with a single charm quark at $\sqrt{s} = 7$ TeV. The CMS experiment measured [11] total cross-sections ($\sigma(W^- + c), \sigma(W^+ + \bar{c})$), absolute and normalized differential cross-sections as a function of the absolute value of the pseudorapidity of the lepton from the W boson decay, and the cross-section ratio $R^c = \sigma(W^+ + \bar{c})/\sigma(W^- + c)$ at a center of mass energy 7 TeV for the fiducial region defined, namely

$$p_T^j > 25 \text{ GeV}, \ |\eta^j| < 2.5, \ |\eta^l| < 2.1,$$
$$p_T^l > 25 \text{ GeV}, \ \text{for} \ W \to \mu\nu_\mu, \quad (1)$$
$$p_T^l > 35 \text{ GeV}, \ \text{for} \ W \to \mu\nu_\mu \ \text{and} \ W \to e\nu_e.$$

There are two different transverse momentum cuts for the charged lepton in the final state. When $p_T^l > 25$ GeV, we only consider the muon decay channel ($W \to \mu\nu_\mu$) for W boson; both muon ($W \to \mu\nu_\mu$) and electron ($W \to e\nu_e$) decay channels for W boson are considered, when $p_T^l > 35$ GeV. This study is organized as follows: in Section 2, we present our results for various latest PDF sets and compare these with the CMS measurements of the total cross-section, absolute and normalized differential cross-sections, and ratios, as well as the correlation between the CT14NNLO PDFs and predictions for W+ charm data. In Section 3, we discuss the impact of the CMS W+ charm production 7 TeV data to the CT14NNLO PDFs. In Section 4, we draw our conclusions.

2   Results

In this section, we present a detailed numerical study of the $pp \to W + c + X$ process at the LHC at a center-of-mass energy of 7 TeV at NLO order QCD using the Monte-Carlo numerical calculation program MadGraph

[12] with CT10NNLO [13], CT14NNLO [14], and MSTW2008NNLO [15] PDFs. PDF uncertainties on the theoretical predictions are given at the 68% confidence level (C.L.). We calculate the total cross-section, differential (absolute and normalized) cross-sections, and the cross-section ratio $R^c = \sigma(W^+ + \bar{c})/\sigma(W^- + c)$ with the $W \to l\nu$ decay (where $l = \mu$ or e). In our study, we use the same kinematical cuts as the CMS detector at the LHC at a center-of-mass energy of 7 TeV [11], that are given in section 1; both the factorization and renormalization scales are set to the value of the W boson mass $\mu_R = \mu_F = m_w$; the charm quark mass is considered and is set to 1.550 GeV; strong interaction coupling α_s is set to 0.118, and for electro-weak parameters, the W boson mass is set to 80.385 GeV; Fermi coupling is set to 1.166×10^{-5} GeV^{-2}; related CKM matrix elements are set to as $V^{cd} = 0.225$ and $V^{cs} = 0.974$; the mass of charged light leptons is considered and set to $m_e = 0.511$ MeV and $m_\mu = 105.658$ MeV. At LO, the Feynman diagrams for the hard scattering processes of the W+ charm production $pp \to W + c + X$ are shown in Fig. 1. The main contribution for the cross-sections of W+ charm production comes from strange quark and gluon scattering, the down-quark contribution is strongly Cabibbo suppressed, and the contribution from the bottom quark and gluon scattering is negligible.

2.1   Total cross-section

The total cross-sections $\sigma(W^+ + \bar{c})$ and $\sigma(W^- + c)$ of the production of a W boson in association with a charm quark in pp collisions at $\sqrt{s} = 7$ TeV at NLO QCD are summarized in Table 1. PDF uncertainties are at 68% confidence level (C.L.), that are obtained from the error sets of CT10NNLO, CT14NNLO, and MSTW2008-NNLO. The experimental measurements from CMS col-
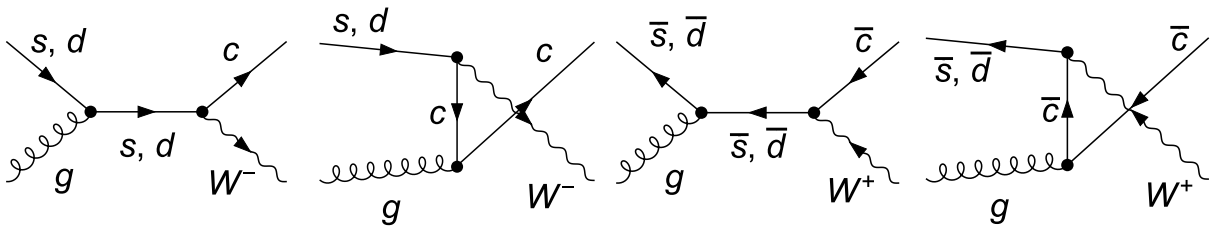

Fig. 1.   Possible tree-level diagrams at partonic level for W+ charm production.

Table 1.   Total cross-section of $\sigma(pp \to W + c) \times B(W \to l\nu)$.

PDF sets	$\sigma(pp \to W + c) \times B(W \to l\nu)$/pb	
	$p_T^l > 25$ GeV	$p_T^l > 35$ GeV
CT10NNLO	$108.1^{+6.6\%}_{-5.5\%}$	$86.4^{+6.7\%}_{-5.5\%}$
CT14NNLO	$100.4^{+7.1\%}_{-10.0\%}$	$80.1^{+7.2\%}_{-10.1\%}$
MSTW2008NNLO	$98.5^{+2.1\%}_{-2.6\%}$	$78.7^{+2.1\%}_{-2.6\%}$
CMS	$107.7 \pm 3.1\%$ (stat.) $\pm 6.4\%$ (syst.)	$84.1 \pm 2.4\%$ (stat.) $\pm 5.8\%$ (syst.)

laboration at the LHC at a center-of-mass energy of 7 TeV [11] are also included in this table. The comparison between theory predictions based on various PDF sets and experimental measurements are illustrated in Fig. 2. The predictions obtained with the CT10NNLO PDFs are in agreement with CMS measurements. The predictions obtained with CT14NNLO agree with CMS measurements within the uncertainty range. The prediction obtained with MSTW2008NNLO is less favored. Those differences in the size of the PDF uncertainties depend on a different methodology, and the parametrization of the $s(x, Q)$ PDF used by different PDF sets.

Our MadGraph calculations of the d, $\bar{d}$, s, and $\bar{s}$ quarks contributions (in pb) to the LO $W+$ charm total cross-sections with NNLO PDFs for the leptonic decay channel $W \rightarrow e\nu$ are shown in Table 2. The strange quark contributes the most to this $W+$ charm production. With regard to the parametrization of the strange-quark content of the proton, CTEQ-TEA and MSTW2008 PDF groups make different assumptions in their global fits. In CT10NNLO and CT14NNLO, the strange quark is parameterized symmetrically $s = \bar{s}$, and in MSTW2008, it is parameterized asymmetrically, $s - \bar{s} \neq 0$. Hence, corresponding theoretical predictions differ accordingly. For

MSTW2008, the production of $W^+ + c$ is slightly larger than the $W^+ + \bar{c}$, as expected because of the $s - \bar{s}$ asymmetry. Because of the dominance of the d quark over the $\bar{d}$-quark in the proton, the production of $W^- + c$ is larger than $W^+ + \bar{c}$. The numbers in brackets correspond to $p_T^l > 35$ GeV.

2.2 Absolute and normalized differential cross-section

The absolute and normalized differential cross-sections are obtained by MadGraph using the same setup as the CMS collaboration at the LHC and a center-of-mass energy of 7 TeV. In Fig. 3 and Fig. 4, we compare the absolute and normalized differential cross-sections in bins of lepton pseudo-rapidity with CMS measurements. The absolute and normalized differential cross-sections with PDF uncertainty at 68% C.L. are summarized in Tables 3 and 4, and the CMS 7 TeV measurement with statistical and systematic uncertainty is given in the last column. There is good agreement between theoretical predictions and measured distributions. The comparisons among predictions from various PDFs may lead to different conclusions. For instance, the predictions based on CT14NNLO and MSTW2008NNLO PDFs are smaller than the predic-
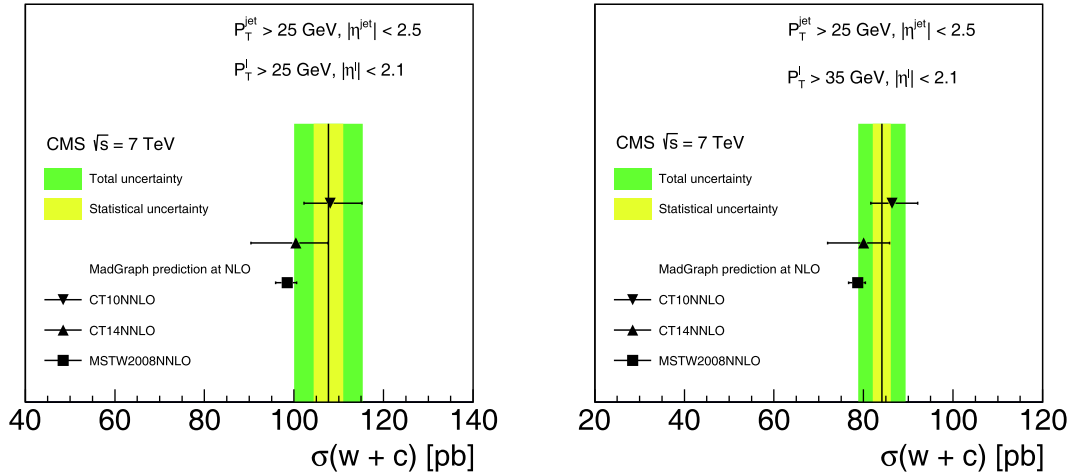

Fig. 2.   (color online) Comparison of theoretical predictions for total cross-section $\sigma(W+c)$ computed with MadGraph using the CT10NNLO, CT14NNLO, and MSTW2008NNLO PDFs with CMS measurements. The left figure contains the prediction for the lepton from W boson decay with $p_T^l > 25$ GeV, while the right figure is for the case $p_T^l > 35$ GeV. The solid vertical line shows the central value of the measurement, the inner error band corresponds to the statistical uncertainty, and the outer error band to the sum in quadrature of the statistical and systematic uncertainties.

Table 2.   LO contributions of d, $\bar{d}$, s and $\bar{s}$ quarks to $\sigma(pp \rightarrow W+c) \times B(W \rightarrow l\nu)$ within the kinematic region $p_T^{\text{jet}} > 25$ GeV, $|\eta^{\text{jet}}| < 2.5$, lepton pseudorapidity range $|\eta_l| < 2.1$ and $p_T^l > 25(35)$ GeV.

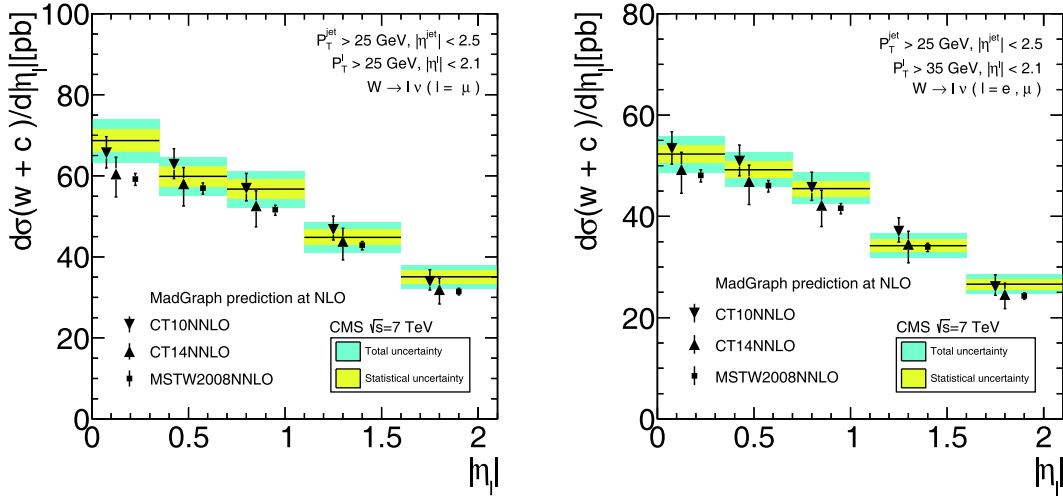| Subprocess	CT10NNLO	CT14NNLO	MSTW2008NNLO
$\bar{s} + g \rightarrow W^+ + \bar{c}$	35.82(28.72)	32.85(26.28)	31.59(25.49)
$\bar{d} + g \rightarrow W^+ + \bar{c}$	2.33(1.89)	2.37(1.92)	2.43(1.96)
$s + g \rightarrow W^- + c$	35.85(28.78)	32.89(26.32)	32.49(26.15)
$d + g \rightarrow W^- + c$	4.50(3.73)	4.58(3.78)	4.66(3.86)

Fig. 3.　(color online) Comparison of theoretical predictions for differential cross-sections, $\mathrm{d}\sigma(W+c)/\mathrm{d}|\eta_l|$, as a function of absolute value of pseudorapidity of lepton from W-boson decay, with CMS measurements. Theoretical predictions at NLO are calculated using MadGraph with CT10NNLO, CT14NNLO and MSTW2008NNLO PDFs. The left figure shows the predictions for the lepton from W boson decay with $p_T^l > 25$ GeV, and the right with $p_T^l > 35$ GeV. Error bars on theoretical predictions show 68% C.L..
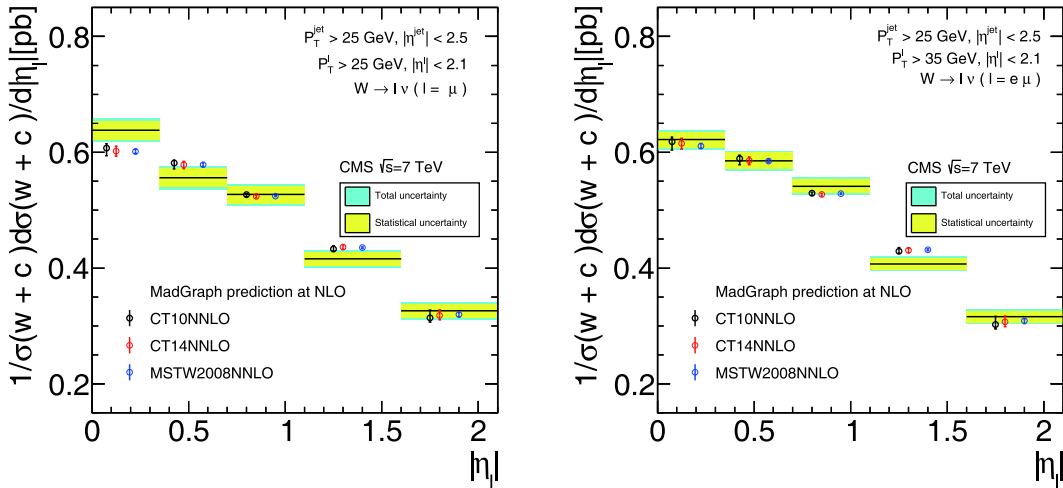

Fig. 4.　(color online) Comparison of theoretical predictions for normalized differential cross-sections, $\mathrm{d}\sigma(W+c)/\sigma\mathrm{d}|\eta_l|$, as a function of absolute value of pseudorapidity of lepton from W-boson decay, with CMS measurements. Theoretical predictions at NLO are calculated using MadGraph with CT10NNLO, CT14NNLO and MSTW2008NNLO PDFs. The left figure shows the predictions for the lepton from the W boson decay with $p_T^l > 25$ GeV, and the right with $p_T^l > 35$ GeV.

tions based on CT10NNLO PDFs, and PDF uncertainties of CT14NNLO PDFs are much larger than the PDF uncertainties of CT10NNLO and MSTW2008NNLO.

2.3　Charged cross-section ratio

We calculated total ($\sigma(W^- + c), \sigma(W^+ + \bar{c})$) and differential (absolute and normalized) cross-sections independently under the same conditions in Subsections 2.1 and 2.2. The CMS[11] collaboration introduced the charged cross-section ratio,

$$R^c = \frac{\sigma(W^+ + \bar{c})}{\sigma(W^- + c)}. \qquad (2)$$

The advantage of using this ratio is that many of the theoretical and experimental uncertainties can cancel. The comparison of the total cross-section ratio and differential cross-section ratio with PDF uncertainty at 68% C.L. with CMS data are shown in Fig. 5 and Fig. 6, the left column corresponds to $p_T^l > 25$ GeV, and right one corresponds to $p_T^l > 35$ GeV. The total cross-section ratio and differential cross-section ratio are also summarized in Table 5 and Table 6. From Tables 5 and 6, we see that the total cross-section ratio, differential cross-section ratio, and the associated PDF uncertainties are different for the CT10, CT14, and MSTW2008 PDF sets. These differences arise from the parametrization assumptions in each

Table 3.   Theory predictions of differential cross-sections $\mathrm{d}\sigma(pp \to W + c) \times B(W \to l\nu)/\mathrm{d}|\eta^l|$ with PDF uncertainty at 68% C.L., last three column for CMS 7 TeV measurement with statistical and systematic uncertainty.

		$p_T^l > 25$ GeV		
$|\eta^l|$	CT10NNLO	CT14NNLO	MSTW2008NNLO	CMS measurement
[0,0.35]	$65.7^{+6.1\%}_{-5.7\%}$	$60.5^{+6.8\%}_{-9.4\%}$	$59.2^{+2.3\%}_{-2.7\%}$	$68.7 \pm 3.9\% \pm 6.7\%$
[0.35,0.7]	$62.8^{+6.2\%}_{-5.6\%}$	$58.1^{+6.9\%}_{-9.5\%}$	$57.0^{+2.3\%}_{-2.7\%}$	$59.9 \pm 4.2\% \pm 6.7\%$
[0.7,1.1]	$56.9^{+6.4\%}_{-5.5\%}$	$52.6^{+7.0\%}_{-9.8\%}$	$51.6^{+2.2\%}_{-2.6\%}$	$56.7 \pm 4.2\% \pm 6.7\%$
[1.1,1.6]	$46.8^{+7.0\%}_{-5.7\%}$	$43.8^{+7.4\%}_{-10.4\%}$	$42.9^{+2.2\%}_{-2.7\%}$	$44.8 \pm 4.2\% \pm 7.1\%$
[1.6,2.1]	$33.9^{+8.5\%}_{-6.2\%}$	$32.0^{+8.7\%}_{-11.3\%}$	$31.5^{+2.4\%}_{-2.9\%}$	$35.1 \pm 4.8\% \pm 6.8\%$
		$p_T^l > 35$ GeV		
$|\eta^l|$	CT10NNLO	CT14NNLO	MSTW2008NNLO	CMS measurement
[0,0.35]	$53.4^{+6.2\%}_{-5.8\%}$	$49.2^{+6.9\%}_{-9.5\%}$	$48.1^{+2.3\%}_{-2.7\%}$	$52.3 \pm 3.3\% \pm 6.1\%$
[0.35,0.7]	$50.9^{+6.3\%}_{-5.7\%}$	$46.9^{+6.9\%}_{-9.7\%}$	$46.1^{+2.3\%}_{-2.7\%}$	$49.2 \pm 3.3\% \pm 6.1\%$
[0.7,1.1]	$45.7^{+6.6\%}_{-5.6\%}$	$42.2^{+7.0\%}_{-10.0\%}$	$41.6^{+2.2\%}_{-2.6\%}$	$45.5 \pm 3.3\% \pm 5.9\%$
[1.1,1.6]	$37.1^{+7.2\%}_{-5.7\%}$	$34.5^{+7.5\%}_{-10.6\%}$	$34.0^{+2.2\%}_{-2.7\%}$	$34.2 \pm 3.5\% \pm 6.1\%$
[1.6,2.1]	$26.1^{+8.9\%}_{-6.3\%}$	$24.6^{+9.0\%}_{-11.4\%}$	$24.3^{+2.4\%}_{-3.0\%}$	$26.6 \pm 3.8\% \pm 6.4\%$

Table 4.   Theory predictions of normalized differential cross-sections $(1/\sigma(W + c))\mathrm{d}\sigma(W + c)/\mathrm{d}|\eta|$ with PDF uncertainty at 68% C.L., last column depicts CMS 7 TeV measurement with statistical and systematic uncertainty.

		$p_T^l > 25$ GeV		
$|\eta^l|$	CT10NNLO	CT14NNLO	MSTW2008NNLO	CMS measurement
[0,0.35]	$0.607^{+1.2\%}_{-2.2\%}$	$0.602^{+1.4\%}_{-1.5\%}$	$0.601^{+0.7\%}_{-0.6\%}$	$0.638 \pm 2.5\% \pm 1.9\%$
[0.35,0.7]	$0.581^{+0.9\%}_{-1.7\%}$	$0.578^{+1.1\%}_{-1.2\%}$	$0.578^{+0.5\%}_{-0.4\%}$	$0.556 \pm 2.9\% \pm 2.2\%$
[0.7,1.1]	$0.527^{+0.3\%}_{-0.7\%}$	$0.524^{+0.4\%}_{-0.5\%}$	$0.524^{+0.2\%}_{-0.2\%}$	$0.527 \pm 2.8\% \pm 2.1\%$
[1.1,1.6]	$0.433^{+1.3\%}_{-0.8\%}$	$0.436^{+0.8\%}_{-0.9\%}$	$0.435^{+0.3\%}_{-0.4\%}$	$0.416 \pm 2.9\% \pm 2.2\%$
[1.6,2.1]	$0.314^{+4.2\%}_{-2.3\%}$	$0.318^{+3.0\%}_{-2.5\%}$	$0.320^{+1.1\%}_{-1.3\%}$	$0.326 \pm 3.7\% \pm 2.8\%$
		$p_T^l > 35$ GeV		
$|\eta^l|$	CT10NNLO	CT14NNLO	MSTW2008NNLO	CMS measurement
[0,0.35]	$0.618^{+1.3\%}_{-2.3\%}$	$0.615^{+1.5\%}_{-1.6\%}$	$0.611^{+0.7\%}_{-0.6\%}$	$0.622 \pm 2.1\% \pm 1.6\%$
[0.35,0.7]	$0.589^{+1.0\%}_{-1.8\%}$	$0.586^{+1.1\%}_{-1.3\%}$	$0.585^{+0.6\%}_{-0.5\%}$	$0.585 \pm 2.4\% \pm 1.7\%$
[0.7,1.1]	$0.529^{+0.4\%}_{-0.7\%}$	$0.527^{+0.4\%}_{-0.5\%}$	$0.528^{+0.3\%}_{-0.2\%}$	$0.541 \pm 2.2\% \pm 1.7\%$
[1.1,1.6]	$0.429^{+1.4\%}_{-0.8\%}$	$0.431^{+0.9\%}_{-1.0\%}$	$0.432^{+0.4\%}_{-0.4\%}$	$0.407 \pm 2.5\% \pm 2.0\%$
[1.6,2.1]	$0.302^{+4.7\%}_{-2.5\%}$	$0.307^{+3.4\%}_{-2.7\%}$	$0.309^{+1.3\%}_{-1.5\%}$	$0.316 \pm 3.2\% \pm 2.2\%$

global analysis. For example, the CT10 and CT14 PDF sets assume $s(x,Q) = \bar{s}(x,Q)$, cross-section ratios almost exclusively are determined by the $d - \bar{d}$ asymmetry and with a very small PDF uncertainty. In contrast, the MSTW08 PDF set assumes asymmetric strangeness $s(x,Q) - \bar{s}(x,Q) \neq 0$, that yields a larger PDF uncertainty in the prediction.

2.4   Correlation between the CT14NNLO and predictions for $W+$ charm data

One way to determine the sensitivity of a specific data point to some PDF $f_i(x,Q)$ at a given x and Q is to compute a correlation cosine between the theoretical prediction for this point and the PDFs of various flavors [16 −18]. Therefore, we will study the correlations between CT14NNLO PDFs of various flavors at specific x and each data point of CMS 7 TeV $W+$ charm production with transverse momentum of the charged lepton from W boson decay at the $p_T^l > 35$ GeV region. However, first we briefly provide the definition of the correlation cosine. If there are two variables $X(\vec{a}_j)$ and $Y(\vec{a}_j)$ in the parameter space, where a_j are the PDF parameters, then the cor-
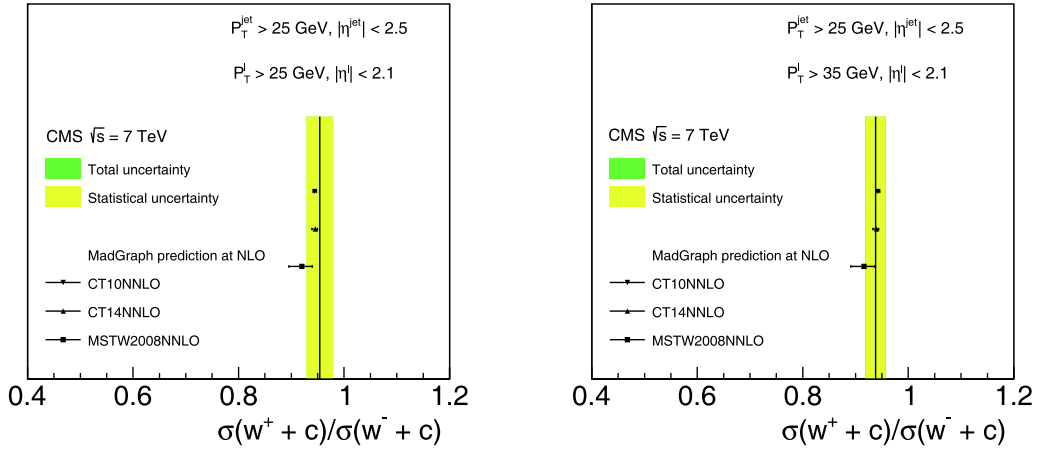
Fig. 5.   (color online) Comparison of theoretical prediction of total cross-section ratio $\sigma(W^+ + \bar{c})/\sigma(W^- + c)$ for three different PDF sets with CMS measurements.
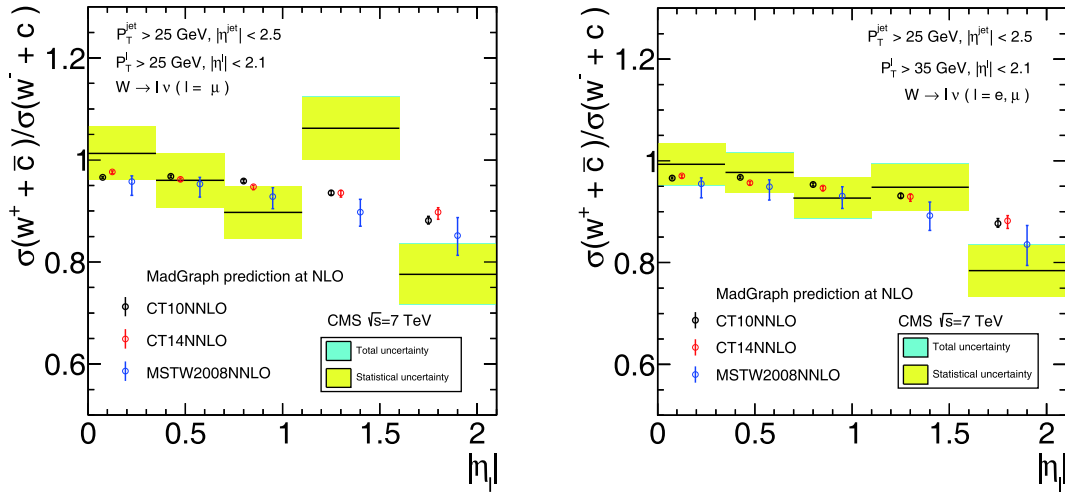

Fig. 6.   (color online) Comparison of theoretical prediction of differential cross-section ratio for three different PDF sets with CMS data.

Table 5.   Theoretical prediction of total cross-section ratio of $\sigma(W^+ + \bar{c})/\sigma(W^- + c)$

	$\sigma(W^+ + \bar{c})/\sigma(W^- + c)$	
PDF sets	$p_T^l > 25$ GeV	$p_T^l > 35$ GeV
CT10NNLO	$0.944^{+0.3\%}_{-0.3\%}$	$0.942^{+0.4\%}_{-0.3\%}$
CT14NNLO	$0.946^{+0.4\%}_{-0.7\%}$	$0.940^{+0.4\%}_{-0.7\%}$
MSTW2008NNLO	$0.920^{+2.2\%}_{-2.7\%}$	$0.916^{+2.3\%}_{-2.7\%}$
CMS	$0.954 \pm 2.5\%$ (stat.) $\pm 0.4\%$ (syst.)	$0.938 \pm 2.0\%$ (stat.) $\pm 0.6\%$ (syst.)

relation cosine can be expressed as:

$$\cos\phi = \frac{\vec{\nabla}X \cdot \vec{\nabla}Y}{|\vec{\nabla}X||\vec{\nabla}Y|}, \qquad (3)$$

where $\vec{\nabla}X$ and $\vec{\nabla}Y$ are gradient of the variables $X(a_j)$ and $Y(a_j)$. For $X(a_i)$, ith component of gradient vector is

$$(\vec{\nabla}X)_j = \frac{\partial X}{\partial a_j} = \frac{1}{2}(X^+(a_j) - X^-(a_j)), \qquad (4)$$

where $X^+(a_j)$ and $X^-(a_j)$ are computed from the two sets of PDFs along the positive and negative direction of the i-th eigenvector. The quantity $\cos\phi$ characterizes whether the variables X and Y are correlated ($\cos\phi \sim 1$), anti-correlated ($\cos\phi \sim -1$), or not correlated ($\cos\phi \sim 0$).

Figure 7 shows the correlation cosine between each data point and CT14NNLO PDF flavors at $Q = 1.3$ GeV and $Q = 100$ GeV. CMS 7 TeV $W+$ charm data contains 17 data points, and thus there are 17 lines for certain fla-

Table 6.   Theoretical prediction of differential cross-section ratio with PDF uncertainty at 68% C.L., last column depicts CMS 7 TeV measurement with statistical and systematic uncertainty.

		$p_T^l > 25$ GeV		
$|\eta^l|$	CT10NNLO	CT14NNLO	MSTW2008NNLO	CMS measurement
[0,0.35]	$0.966^{+0.2\%}_{-0.2\%}$	$0.977^{+0.2\%}_{-0.4\%}$	$0.958^{+1.2\%}_{-2.8\%}$	$1.013 \pm 5.1\% \pm 0.5\%$
[0.35,0.7]	$0.968^{+0.2\%}_{-0.2\%}$	$0.962^{+0.2\%}_{-0.4\%}$	$0.953^{+1.4\%}_{-2.7\%}$	$0.960 \pm 5.5\% \pm 0.5\%$
[0.7,1.1]	$0.959^{+0.3\%}_{-0.3\%}$	$0.947^{+0.3\%}_{-0.6\%}$	$0.928^{+1.9\%}_{-2.6\%}$	$0.897 \pm 5.7\% \pm 0.9\%$
[1.1,1.6]	$0.935^{+0.5\%}_{-0.4\%}$	$0.935^{+0.5\%}_{-0.9\%}$	$0.898^{+2.8\%}_{-3.1\%}$	$1.062 \pm 5.7\% \pm 1.3\%$
[1.6,2.1]	$0.881^{+1.0\%}_{-0.8\%}$	$0.818^{+1.0\%}_{-1.5\%}$	$0.852^{+4.1\%}_{-4.6\%}$	$0.776 \pm 7.5\% \pm 2.1\%$
		$p_T^l > 35$ GeV		
$|\eta^l|$	CT10NNLO	CT14NNLO	MSTW2008NNLO	CMS measurement
[0,0.35]	$0.966^{+0.2\%}_{-0.2\%}$	$0.970^{+0.2\%}_{-0.4\%}$	$0.955^{+1.2\%}_{-2.9\%}$	$0.993 \pm 4.1\% \pm 0.7\%$
[0.35,0.7]	$0.968^{+0.2\%}_{-0.2\%}$	$0.957^{+0.3\%}_{-0.5\%}$	$0.949^{+1.4\%}_{-2.7\%}$	$0.977 \pm 4.0\% \pm 0.7\%$
[0.7,1.1]	$0.953^{+0.3\%}_{-0.3\%}$	$0.947^{+0.3\%}_{-0.6\%}$	$0.931^{+2.0\%}_{-2.6\%}$	$0.927 \pm 4.3\% \pm 0.9\%$
[1.1,1.6]	$0.931^{+0.5\%}_{-0.5\%}$	$0.930^{+0.6\%}_{-1.0\%}$	$0.892^{+3.0\%}_{-3.3\%}$	$0.948 \pm 4.9\% \pm 1.1\%$
[1.6,2.1]	$0.877^{+1.1\%}_{-0.8\%}$	$0.882^{+1.2\%}_{-1.7\%}$	$0.836^{+4.5\%}_{-5.0\%}$	$0.784 \pm 6.4\% \pm 1.4\%$

vors in Fig. 7. Correlations of $s(x,Q)$ PDF and $g(x,Q)$ PDF with each data point are given at the first row in Fig. 7. Correlations of $u(x,Q)$ PDF and $\bar{u}(x,Q)$ PDF with each data point are given at the second row in Fig. 7. Finally, correlations of $d(x,Q)$ PDF and $\bar{d}(x,Q)$ PDF with each data point are given at the third row in Fig. 7. In each subfigure, the correlation between one of the PDF flavors with each data point is distinguished by different type of line. Solid, long-dashed-dotted, dotted, short-dashed, and short-dashed-dotted lines correspond to correlation of differential cross-section, differential cross-section ratio, normalized differential cross-section, total cross-section and total cross-section ratio data, respectively. As we discussed in Section 2, differential cross-section, differential cross-section ratio, and normalized differential cross-section data has included five data points that are measured by five rapidity bin ranges. The lines with a darker color correspond to the higher rapidity bin range.

In the case of the total cross-section, differential cross-section and ratio, $s(x,Q)$ PDF correlations are most significant ($\cos\phi \sim 1$) at x from few times 10^{-2} to few times 10^{-1}, when $Q = 1.3$ GeV and $Q = 100$ GeV, respectively. However, at other x range, the $s(x,Q)$ PDFs correlation is not very strong. There are no clear relations between the rapidity bin range and correlation cosine, however it can be seen from two subfigures at the first row that each data point in various rapidity bins has a strong correlation with $s(x,Q)$ PDF at the x-region mentioned above. There is other information for the normalized differential cross-section, which includes five data points that are partially correlated and partially anti-correlated, and represented with each flavor, as illustrated in

each subfigure of Fig. 7 with five dashed-lines (red or blue) that are inconsistent with other types of lines. Correlated data points prefer PDFs to become larger, and anti-correlated data points prefer PDFs to become smaller. Hence, the impact of normalized cross-section data on PDFs is neutralized. Not considering the correlations with normalized cross-section data, the d(anti) quark and u(anti) PDFs are anti-correlated at $x < 0.4$ region, and small at all x-regions when both $Q = 1.3$ GeV and $Q = 100$ GeV, which can be seen in subfigures in the second and third rows of Fig. 7. Thus, those data points without normalized cross-section data prefer d(anti) quark and u(anti) PDFs to become smaller in the $x < 0.4$ region. Gluon's correlation is likewise miniscule in the x-region, which can be seen in the subfigures in the first row of Fig. 7. One can conclude that CMS 7 TeV $W+$ charm data have larger impact on $s(x,Q)$ PDF in CT14NNLO than other flavors.

3   Using EPUMP to study the impact of $W+$ charm data on CT14NNLO PDFs

The study cited in Ref. [19] presented a software package, ePump (error PDF updating method package), that can be used to update or optimize a set of PDFs, including the best-fit PDF set and error PDFs, and to update any other set of observables. Furthermore, Ref. [20] and Ref. [21] cite some interesting further studies using ePump. In this section, we use ePump to analyze the impact of CMS 7 TeV $W+$ charm production measurements on the CT14NNLO PDFs. To update CT14NNLO PDFs, we use the CMS 7 TeV total cross-section (one data
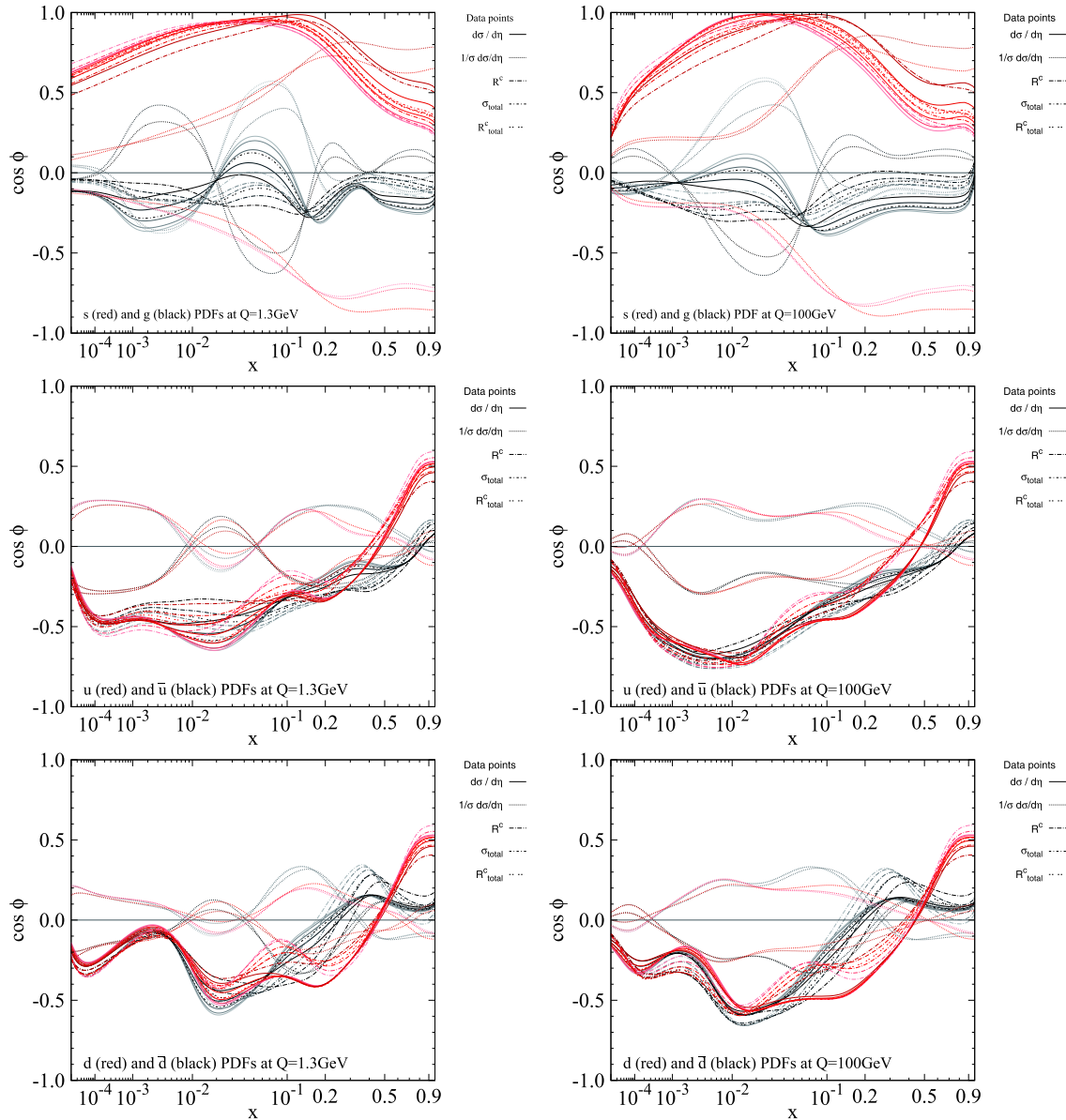
Fig. 7.   (color online) Correlation $\cos\phi$ between CT14NNO PDFs at the specific x value on the horizontal axis and CT14NNLO predictions at NLO for CMS 7 TeV $W+$ charm production at $Q = 1.3$ GeV(left panel) and $Q = 100$ GeV(right panel).

point), differential cross-section (five data points), total cross-section ratio (one data point) and differential cross-section ratio (five data points), as well as combined data sets and their NLO QCD predictions from MadGraph as ePump inputs. CT14NNLO+sig, CT14NNLO+dsig, CT14NNLO+R, CT14NNLO+dR, and CT14NNLO+Wc in Figs. 8-9 are the ePump-updated PDFs by total cross-section data, differential cross-section data, total cross-section ratio data, differential cross-section ratio data, and combined CMS 7 TeV $W+$ charm data. The weight factor for each data is three in our ePump studies. A weight larger than one is equivalent to having more data points with the same experimental uncertainties or, alternatively, to reducing the experiment uncertainties by a factor of the

square root of the weight. In the combined data, we excluded the normalized differential cross-section data to avoid double counting. After updating, the relative changes in CT14NNLO ensembles are best visualized by comparing their PDF error band and PDF ratio, in which ratio plot is obtained by dividing the error set and best fit of updated PDFs by the best fit of original CT14NNLO PDFs. In Figs. 8-9, we show the impact of $W + c$ data and combined data on CT14NNLO PDFs, namely, Comparisons of CT14NNLO PDF (light blue) and ePump-updated PDFs CT14NNLO+sig (orange), CT14NNLO+dsig (magenta), CT14NNLO+R (purple), CT14NNLO+dR (green), and CT14NNLO+Wc(blue) at $Q = 1.3$ GeV (left column) and $Q = 100$ GeV (right column). Flavors
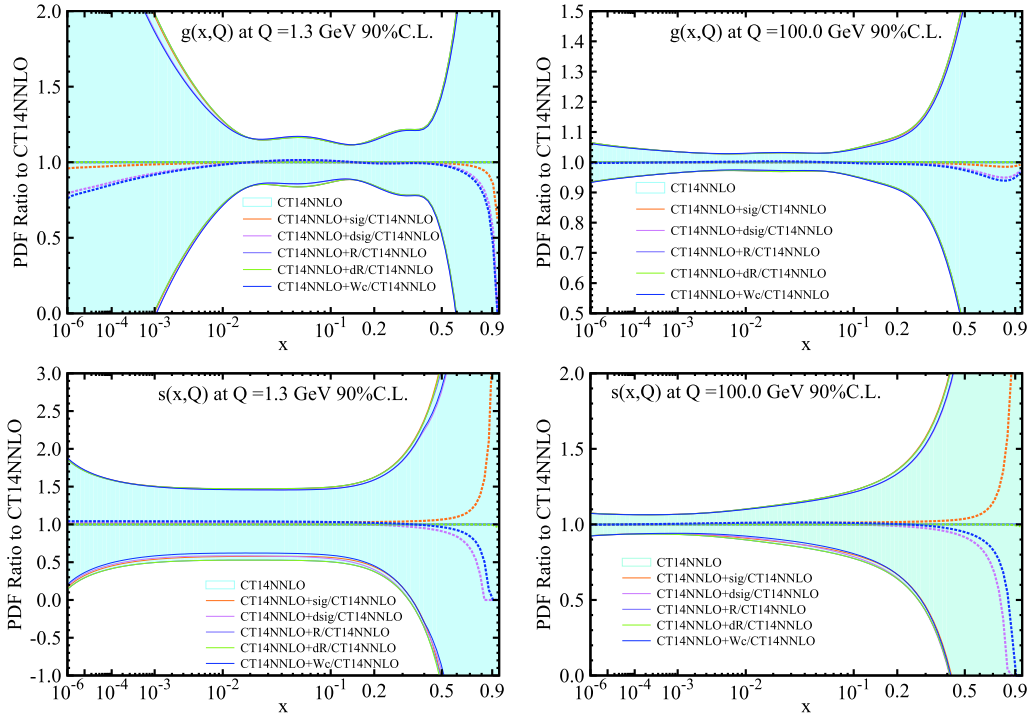
Fig. 8. (color online) Comparison of 90% C.L. $g(x,Q)$ PDF (first row) and $s(x,Q)$ PDF (second row) uncertainties from CT14NNLO and CT14NNLO+sig, CT14NNLO+dsig, CT14NNLO+R, CT14NNLO+dR, CT14NNLO+Wc. Shaded area represents error bands of CT14NNLO PDFs. The area between the solid line represents error bands of ePump-updated PDFs, which are distinguished by different colors, and the dotted line depicts the best fit PDFs. Both best fit PDFs and error bands are normalized to the corresponding central CT14NNLO PDFs.
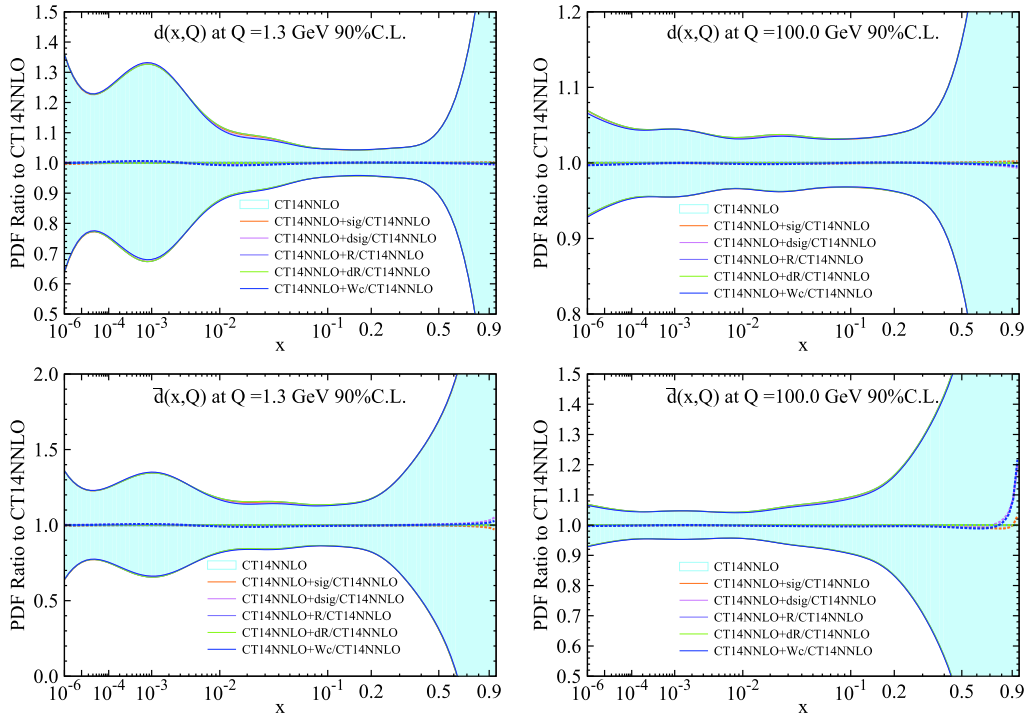

Fig. 9. (color online) Comparison of 90% C.L. $d(x,Q)$ PDF (first row) and $\bar{d}(x,Q)$ PDF (second row) uncertainties from CT14NNLO and CT14NNLO+sig, CT14NNLO+dsig, CT14NNLO+R, CT14NNLO+dR, CT14NNLO+Wc. Shaded area represents error bands of CT14NNLO PDFs. The area between the solid line represents error bands of ePump-updated PDFs, which are distinguished by different colors, and the dotted line depicts the best fit PDFs.

$g(x,Q)$, $s(x,Q)$, $u(x,Q)$, $\bar{u}(x,Q)$, $d(x,Q)$, and $\bar{d}(x,Q)$ are shown. The PDF uncertainty bands are 90% C.L..

The change in $g(x,Q)$ PDF mostly comes from the differential cross-section data. The changes in the best fit value and uncertainty of the ePump-updated $g(x,Q)$ PDF are visualized in the first row of Fig. 8, compared to CT14NNLO PDFs. The central value of the updated $g(x,Q)$ PDF in the range $10^{-1} < x < 0.5$ remains almost unchanged, and it is increased slightly in the range $10^{-2} < x < 10^{-1}$, compared to CT14NNLO for $Q = 1.3$ GeV, whereas it is decreased by large factors for $x < 10^{-3}$ and $x > 0.5$. For $Q = 100$ GeV, the central value of the updated $g(x,Q)$ PDF in the range $x < 0.5$ remains almost unchanged, and some variations of the best fit $g(x,Q)$ in the region $x > 0.5$ are observable. The $g(x,Q)$ PDF is not efficiently determined in very small and a very large x-regions, however all remain within the error bands of the PDFs. The error band of the updated $g(x,Q)$ PDF is slightly reduced in the range $10^{-2} < x < 10^{-1}$ for $Q = 1.3$ GeV. In other regions, the updated $g(x,Q)$ PDFs uncertainty bands are comparable to that of CT14NNLO.

The $s(x,Q)$ PDF is most sensitive to CMS 7 TeV $W+$ charm data. Total and differential cross-section data are responsible for most of the changes in central values and uncertainties of the updated $s(x,Q)$ PDF. The changes in the central value and uncertainty of the ePump-updated $s(x,Q)$ PDF is visualized in the second row of Fig. 8, compared to CT14NNLO PDFs. After updating the PDF by combined data, the best fit $s(x,Q)$ PDF is increased slightly in the region $x < 0.4$ for $Q = 1.3$ GeV. There is a large change of the $s(x,Q)$ PDF in the region $x > 0.5$ for both $Q = 1.3$ GeV and $Q = 100$ GeV, however well within the error bands of PDFs.

The LO contributions of s, $\bar{s}$, d, $\bar{d}$ quarks to the $W+$ charm production cross-section are shown in Table 2. d and $\bar{d}$ quarks contributions are significantly small relative to s and $\bar{s}$ quarks contributions, because $dg \rightarrow W^- + c$ and $\bar{d}g \rightarrow W^+ + \bar{c}$ processes are suppressed by the CKM

matrix element. However, we cannot neglect d and $\bar{d}$ quark contributions to the $W+$ charm cross-section, the d quark contribution is about 11% of the $W^- + c$ productions cross-section and the $\bar{d}$ quark contribution is about 6% of the $W^- + c$ productions cross-section. Therefore, CMS 7 TeV $W+$ charm data can have an impact on both $d(x,Q)$ and $\bar{d}(x,Q)$ PDFs. Fig. 9 shows the changes in central values and uncertainties of the updated $d(x,Q)$ and $\bar{d}(x,Q)$ PDFs for both $Q = 1.3$ GeV and $Q = 100$ GeV. Most of the changes in $d(x,Q)$ and $\bar{d}(x,Q)$ PDFs come from total and differential cross-section data of CMS 7 TeV $W+$ charm production. After updating the CT14NNLO PDFs by combined data, the error band of $d(x,Q)$ PDF is slightly reduced in the region $10^{-2} < x < 10^{-1}$ for both $Q = 1.3$ GeV and $Q = 100$ GeV. The best fit $d(x,Q)$ PDF decreased a little bit in this region. For both $Q = 1.3$ GeV and $Q = 100$ GeV, the central value and uncertainty of the ePump-updated $\bar{d}(x,Q)$ PDF are close to that of CT14NNLO in the region $x < 0.5$. The best fit $\bar{d}(x,Q)$ PDF is increased significantly in the region $x > 0.5$, however well within the error bands of PDFs.

At the LO, u quark does not contribute to the $W+$ charm production cross-section, however it does so beyond the LO. In our ePump study, we employ the theoretical prediction of the $W+$ charm production cross-section at NLO QCD. Therefore, we compare the ePump-updated PDFs via CMS 7 TeV $W+$ charm data and CT14NNLO PDFs to see the impact on $u(x,Q)$ and $\bar{u}(x,Q)$ PDFs in CT14NNLO for both $Q = 1.3$ GeV and $Q = 100$ GeV. We found that the central value and uncertainties of the ePump updated $u(x,Q)$ and $\bar{u}(x,Q)$ are almost unchanged.

In Fig. 10, we compared the $s(x,Q)$ PDF from CT14NNLO, and ePump-updated $s(x,Q)$ PDF from combined CMS 7 TeV $W+$ charm data with weights three and ten. Fig. 10 shows that the $s(x,Q)$ PDF error band greatly decreases at $x < 0.4$ for $Q = 1.3$ GeV and $Q = 100$ GeV when the weight factor is increased from three to ten. The
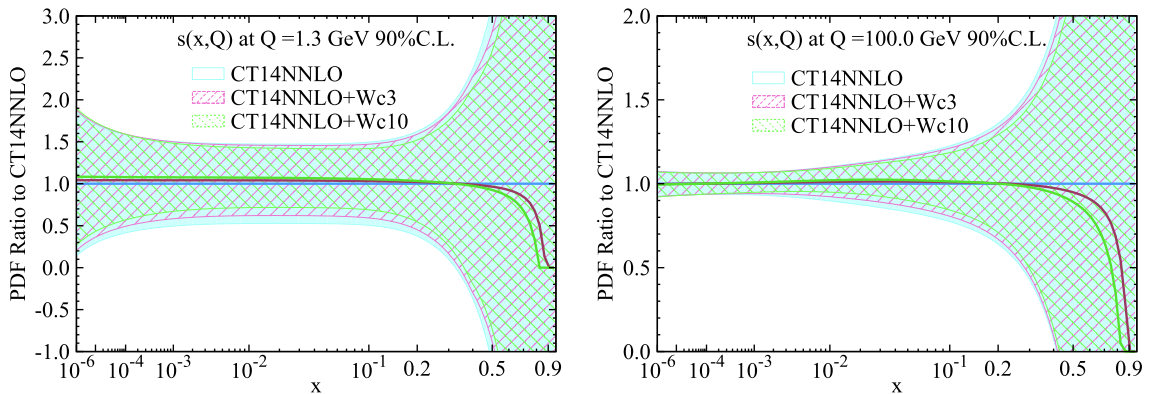

Fig. 10.   (color online) Comparison of 90% C.L. $s(x,Q)$ PDF uncertainties at $Q = 1.3$ GeV and $Q = 100$ GeV from CT14NNLO and CT14NNLO+Wc3 and CT14NNLO+Wc10 corresponding to $s(x,Q)$ PDF updated by combined CMS 7 TeV $W+$ charm data with weight factors three and ten.

best fit $s(x, Q)$ PDF increases in the region $x < 0.1$. At large x, the best fit $s(x, Q)$ PDF decreases significantly for both $Q = 1.3$ GeV and $Q = 100$ GeV, however remains well within the error bands of PDFs.

Using ePump [19], we updated CT14NNLO PDFs. One might want to know how the inclusion of the CMS 7 TeV $W+$ charm data in the global PDF fits would modify the prediction and uncertainties for any other set of observables including the original observables that were

used for updating the CT14NNLO PDFs. ePump can also directly update predictions and uncertainties for any observables after including new data. In Fig. 11, we compare the predictions from CT14NNLO PDFs and CT14NNLO+Wc PDFs, obtained by updating the CT14NNLO with the CMS 7 TeV $W+$ charm data using ePump with CMS 7 TeV $W+$ charm data. Fig. 11 shows that the uncertainties decreased after the update, and the predicted central value is also closer to the data.
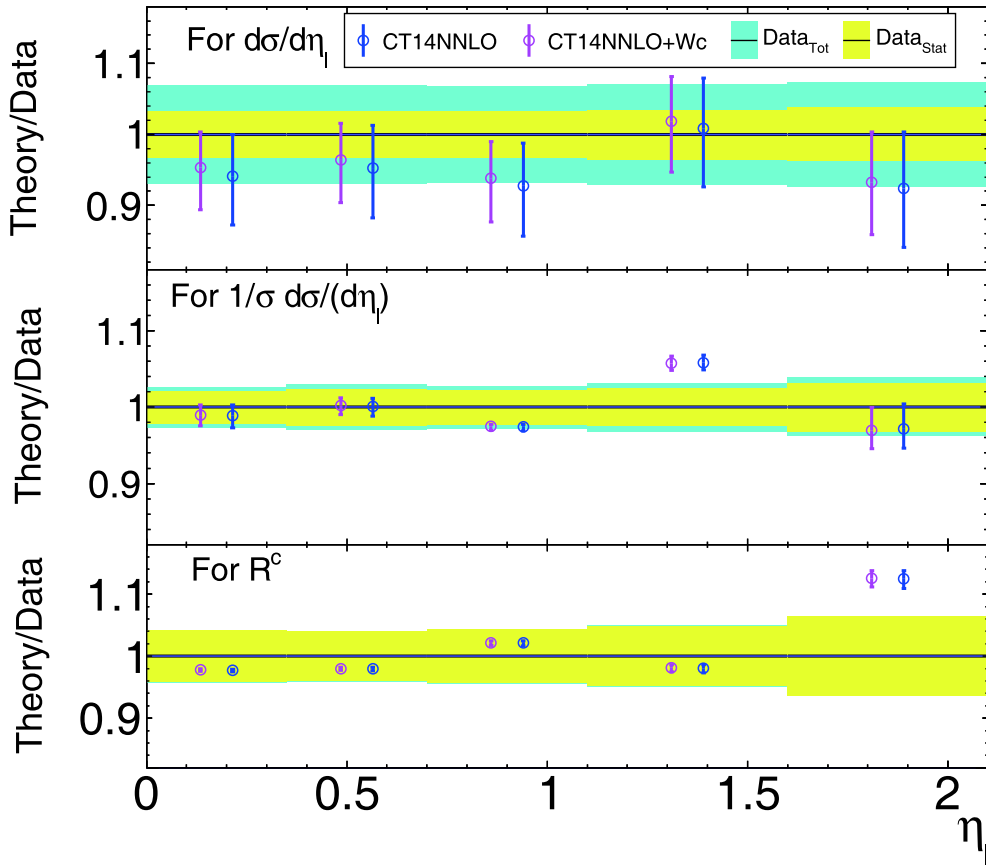

Fig. 11.   (color online) Comparison of data and theoretical predictions obtained from updated and original CT14NNLO PDFs, PDF uncertainty at 68% C.L.

4   Conclusions

In this study, we calculated the total and differential cross-sections and cross-section ratios using the Mad-Graph up to $O(\alpha_s^2)$ with a massive charm quark $m_c = 1.55$ GeV for three NNLO PDF sets: MSTW2008, CT10, and CT14NNLO. Subsequently, we compared the experimental measurements of $W+$ charm production at $\sqrt{s} = 7$ TeV at LHC. In our calculation, we use the same kinematic cuts as experimental measurements: $p_T^{\text{jet}} > 25$ GeV, $|\eta^{\text{jet}}| < 2.5$, and $|\eta_l| < 2.1$ GeV, and two different transverse momentum cuts $p_T^l > 25$ GeV for the $W \to \mu\nu$ chan-

nel and $p_T^l > 35$ GeV for the $W \to \mu\nu$ and $W \to e\nu$ channels. In our calculation, both the factorization and the renormalization scales are set to the value of the W boson mass, and $\alpha_s(M_Z)$ is set to the central value provided by the respective PDF groups. Our results are summarized in Tables 1 - 6 and in Figs. 2 - 6, where the central value of the prediction and the PDF uncertainty are given. The theoretical predictions from various PDFs agree well with experimental measurements. However, there are some differences depending on the PDFs used in the calculations. For example, unlike the assumption in MSTW20018 NNLO PDFs, the CT10 and CT14 assume

$s = \bar{s}$ in the proton, yielding to a total and differential cross-sections ratio dominated by the $d - \bar{d}$ asymmetry. The total and differential cross-sections are larger for the $W^- + c$ production than for $W^+ + c$, because the former process involves a d, whereas the latter involves $\bar{d}$ (sea) antiquark. Hence, both total and differential cross-section ratios are smaller than 1.0.

Fig. 7 shows that the observable from the CMS 7 TeV $W+$ charm production has a strong correlation with the strange (anti) quark PDFs, therefore these measurements also provide a direct constraint on the strange (anti) quark content of the proton.

Furthermore, using the ePump updating method, and CMS 7 TeV $W+$ charm production data at lepton transverse momentum $p_T^l > 35$ GeV, we find that these data sets mainly reduce the $s(x, Q)$ PDF error band and increase magnitude of its best fit in the $x < 0.4$ region for both $Q = 1.3$ GeV and $Q = 100$ GeV. In Fig. 11, we also compare the predictions from CT14NNLO PDFs and CT14NNLO+Wc PDFs.

References

1   W. J. Stirling and E. Vryonidou, Phys. Rev. Lett., **109**: 082002 (2012), arXiv:1203.6781
2   N. Cabibbo, Phys. Rev. Lett., **10**: 531-533 (1963)
3   U. Baur, F. Halzen, S. Keller et al, Phys. Lett. B, **318**(544): 544-548 (1993), arXiv:hep-ph/9308370
4   S. Keller, W. T. Giele, and E. Laenen, Phys. Lett. B, **372**: 141 (1996)
5   H. L. Lai, P. M. Nadolsky, J. Pumplin et al, JHEP, **04**: 089 (2007), arXiv:hep-ph/0702268
6   NuTeV Collaboration, M. Goncharov et al, Phys. Rev. D, **64**: 112006 (2001), arXiv:hep-ex/0102049
7   NuTeV Collaboration, D. Mason et al, Phys. Rev. Lett., **99**: 192001 (2007)
8   T. Aaltonen et al, CDF Collaboration, Phys. Rev. Lett., **100**: 091803 (2008), arXiv:0711.2901
9   V. M. Abazov et al, D0 Collaboration, Phys. Lett. B, **666**: 23-30 (2008), arXiv:0803.2259
10 ATLAS Collaboration, arXiv: 1402.6263
11 S. Chatrchyan et al, CMS Collaboration, JHEP, **02**: 013 (2014), arXiv:1310.1138
12 J. Alwall, M. Herquet, F. Maltoni et al, JHEP, **06**: 128 (2011), arXiv:1106.0522
13 H.-L. Lai, M. Guzzi, J. Huston et al, Phys. Rev. D, **82**: 074024 (2010), arXiv:1007.2241
14 S. Dulat, T.-J. Hou, J. Gao et al, Phys. Rev. D, **93**: 033006 (2016), arXiv:1506.07443
15 A. D. Martin, W. J. Stirling, R. S. Thorne et al, Eur. Phys. J. C, **63**: 189-285 (2009), arXiv:0901.0002
16 J. Pumplin, D. Stump, R. Brock et al, Phys. Rev. D, **65**: 014013 (2001), arXiv:hep-ph/0101032
17 P. M. Nadolsky and Z. Sullivan, eConf C, **010630**: P510 (2001), arXiv:hep-ph/0110378
18 P. M. Nadolsky, H.-L. Lai, Q.-H. Cao et al, Phys. Rev. D, **78**: 013004 (2008), arXiv:0802.0007
19 C. Schmidt, J. Pumplin, and C. P. Yuan, Phys. Rev., **98**: 094005 (2018), arXiv:1806.07950
20 C. Willis, R. Brock, D. Hayden et al, Phys. Rev., **99**: 054004 (2019), arXiv:1809.09481
21 T. J. Hou, Z. Yu, S. Dulat et al, arXiv: 1907.12177